

Supercapacitors from high fructose corn syrup-derived activated carbons

Wenxin Cao, Fuqian Yang*

Materials Program, Department of Chemical and Materials Engineering, University of Kentucky, Lexington, KY 40506, USA

ARTICLE INFO

Article history:

Received 27 February 2018

Received in revised form

2 June 2018

Accepted 4 July 2018

Available online 18 July 2018

Keywords:

Activated carbons

Fructose corn syrup

Hydrothermal carbonization

Supercapacitor

ABSTRACT

Hydrothermal processing and physical activation are used to prepare activated carbons from high fructose corn syrup. The activated carbons are present in spherical shape and possess a high surface area of 1473 m²/g. Both the surface area and micropore fraction increase with the increase of the activation time. Using the prepared activated carbons as electrodes and 6 M KOH aqueous solution as electrolyte, supercapacitor cells of symmetrical type (two electrodes) are constructed. The electrochemical performance of the supercapacitor cells is investigated. The experimental results show the increase of the specific gravimetric capacitance with the increase of the total surface area, suggesting the importance of the activation time in controlling the porous characteristics of the activated carbons and the electrochemical characteristics of the supercapacitor cells made from the activated carbons. The largest specific capacitance and energy density achieved are 168 F/g at an electric current density of 0.2 A/g and 4.2 W h/kg at a power density of 1.5 kW/kg. The micropores play a dominant role in the energy storage of the supercapacitor cells made from the prepared activated carbons.

© 2018 Elsevier Ltd. All rights reserved.

1. Introduction

Electrochemical double layer capacitors (EDLCs), whose energy storage is determined by the accumulation of electric charge at the electrode/electrolyte interface, has attracted great attention because of their high specific power capability, fast charging-discharging rate, long cycle life in comparison with lithium-ion batteries as well as relatively higher energy density than dielectric capacitors [1]. One of the key elements in EDLCs determining the energy storage is the topological structures of electrode, such as specific surface area, pore sizes [2–5], and distribution of pore sizes [6]. Currently, a variety of carbon-based materials have been studied as electrode materials of EDLCs, including carbon nanotubes (CNTs) [7], activated carbons (ACs), templated porous carbons (TPCs) [8,9] and graphene [10–17]. Among the carbon-based materials, ACs with large specific surface area (SSA) (1000–3000 m²/g) and highly porous structure have great potential in the application of EDLCs [18]. However, the electrochemical performance of ACs is dependent on the activation method and the precursors used for the synthesis of ACs.

Biomass, as an important economic, environmental-friendly and natural resource with abundant reserves [19], has potential applications in the devices and systems of energy storage, including lithium-ion batteries [19], lithium sulfur batteries [20,21], and EDLCs [22–28]. There are two important steps in the synthesis of ACs from biomass; one is the pretreatment/carbonization by converting biomass into biochar [29–33], and the other is activation of the carbonized materials at high temperature to form ACs of open porosity and high SSA. There are two basic methods for the activation of carbonized materials; one is physical activation, and the other is chemical activation. Generally, chemical activation is more effective than physical activation, and can lead to the formation of micropores with a great amount of accessible surface areas, while it involves the use of corrosive agents like KOH, and needs extra washing steps to remove the corrosive agents. A variety of ACs have been derived from different biomasses, including hemp [34,35], corncob residue [36], cherry stones [37], coconut kernel pulp [38], etc. Most studies reported in literature have used activation agents during either chemical or physical activation.

High-fructose corn syrup (HFCS), which is a mixture of glucose and fructose, has been extensively used as a liquid sweetener alternative to sucrose (table sugar) in many foods and beverages [39]. Using an iron-based ionic liquid as solvent and a porogenic agent, Lin et al. [40] recently prepared microporous and

* Corresponding author.

E-mail address: fyang2@uky.edu (F. Yang).

mesoporous carbon aerogels from D-fructose via a one-step ionothermal carbonization at 180 °C for 6 h and obtained a high surface area of 1200 m²/g. They prepared a three-electrode system in a 3 M KOH electrolyte solution from the carbon aerogels, and obtained a high specific capacitance of 245 F/g at a current density of 1 A/g. They did not use physical activation to activate the carbon aerogels. There are few studies focusing on the use of fructose to produce ACs for the application in EDLCs, and there is little report on physical self-activation.

Considering the wide availability and environmental acceptability, HFCS was used as a precursor in this work for the synthesis of ACs via hydrothermal carbonization (HTC) process and physical self-activation process. The synthesized ACs were analyzed and used as the electrode material of EDLCs. The electrochemical performance of the EDLCs was investigated in 6 M KOH aqueous solution.

2. Experimental details

The precursor for the HTC process is HFCS55 (Cargill, Wayzata, MN). The HFCS55 is a liquid of light yellow-green color with ~77.1 wt% solid, in which there is ~55 wt% fructose. 70 ml of an aqueous solution consisting of ~10.4 vol% HFCS55 and ~69.6 vol% deionized (DI) water was placed in a Teflon-lined autoclave of 100 ml, which was placed in a pre-heated oven at 493 ± 2 K. A thermocouple of K-type was attached to the Teflon-lined autoclave to monitor the temperature evolution. It took ~2.5 h for the Teflon-lined autoclave with the aqueous solution to reach the temperature of 493 K. The temperature of the Teflon-lined autoclave with the aqueous solution was then maintained at 493 K for 1 h before letting the Teflon-lined autoclave cool down to room temperature in the oven in air. The hydrothermal carbonization of the HFCS 55 took place during the heating and cooling process.

The hydrothermal product was first sonicated at room temperature for 1 h. Using Grade 2 Whatman filter papers (Sigma-Aldrich, St. Louis, MO), the carbonized material was then collected by the filtration method with the use of DI water. The collected carbonized material was dried in an oven at 373 K for 12 h.

Physical self-activation of the carbonized material was performed in a tube furnace (21100 tube furnace, Barnstead Thermolyne Drop., Ramsey, MN) with the passage of nitrogen gas at a temperature of 1123 K for different times. Here, the activation temperature of 1123 K was determined after performing the electrochemical characterization of the carbonized material activated at three different temperatures of 1073, 1123, and 1173 K (see supporting information). Note that no materials, such as CO₂, steam or oxides were used in the activation in contrast to the activation of carbonized materials reported in literature. The ACs were collected in a vial after the furnace was cooled down to room temperature in the nitrogen environment, and then placed in an oven at 373 K overnight. Note that the use of nitrogen gas avoided the burning and oxidation of the carbonized material during the activation and the cooling, respectively.

The morphology and selected area electron diffraction (SAED) patterns of the activated carbons were examined using Field Emission Scanning Electron Microscopy (FESEM) (Tescan MIRA3 LMH) at 10 kV and Transmission Electron Microscopy (TEM) (JEOL 2100-F) at 200 kV. The structures and surface chemistry of the ACs were analyzed by X-ray diffraction (XRD) using a Bruker-AXS D8 Advance equipped with Cu K α radiation ($\lambda = 1.5406$ Å) and Fourier-transform infrared spectroscopy (FTIR) (Thermo Scientific Nicolet iS50 FT-IR spectrometer). To determine the surface area and pores of the activated carbons, the nitrogen adsorption–desorption isotherms were measured by an automated gas adsorption analyzer (Micromeritics surface characterization, Norcross, GA).

Supercapacitor cells of symmetrical type (two-electrodes) were prepared with the ACs as the electrode material, using a Teflon screw two-electrode cell (Swagelok cell). The ACs were first ground and dried in an oven until there was no change in weight, and the ACs of ~1 mg were then placed on the surface of the current collector made from stainless steel to form an electrode. The electrodes were screwed tightly in a Teflon screw two-electrode cell with a 696 glass microfiber filter (VWR International, LLC.) as separator. Considering the wide use of KOH solutions in supercapacitors and the average pore size of ACs, 6 M KOH solution was used as the electrolyte. Note that no binders and additives were used in the preparation of the electrodes, since the preliminary results show that there is no observable difference of specific gravimetric capacities between pure ACs and the same ACs with PTFE binder of 8 wt% (see supporting information).

The electrochemical performance of the AC-based supercapacitor cells was characterized using a VSP 5-channel potentiostat system (BioLogic Science Instruments, Seyssinet-Pariset, France). The potential window for the cyclic voltammetry (CV) measurement was in a range of 0–1 V, and the voltage scanning rate was in a range of 2–100 mV/s. The current densities for the galvanostatic charging and discharging (GC) measurements were in a range of 0.2–10 A/g with the voltage in a range of 0–1 V. The EIS (electrochemical impedance spectroscopy) measurement was recorded in a frequency range of 20 mHz–1 MHz with a sinusoid alternative voltage of 10 mV.

3. Results and discussion

To analyze the effect of the activation time on the topological characteristics of ACs and the electrochemical characteristics of AC-based supercapacitor cells, the prepared ACs are denoted as AC-x. Here, the “x” represents the activation times of 1, 2, 3, and 4 h.

3.1. Materials characterization

Fig. 1 shows SEM images of the ACs formed via the HTC process and the physical self-activation. It is evident that the hydrothermal carbonization of HFCS55 led to the formation of uniform and homogeneous carbon spheres with an average size of ~1 μ m (Fig. 1a). There are a series of hydrolysis, dehydration, and decarboxylation reactions during the HTC process, which lead to the nucleation and growth of carbon spheres.

Fig. 1b–d shows SEM images of the ACs with the activation times of 2, 3, and 4 h, respectively. The activation of the carbonized spheres at 1123 K did not cause any growth and significant topological change of the carbon spheres, while it caused slight decrease of the diameter of carbon spheres and local solid-state sintering. Such behavior is due to the surface interaction between carbon spheres, which causes the migration of atoms and molecules.

Fig. 2 shows TEM images of the carbon particles heat-treated with different activation times. The activated carbon particles are presented in spherical shape in accord with the SEM images shown in Fig. 1b–d. Aggregated and stacked AC spheres are observed in all the TEM images, suggesting the neck formation associated with local solid sintering. There is no significant difference between the diameters (~0.8 μ m) of the AC spheres. The embedded SAED pattern in Fig. 2d reveals that the AC spheres are amorphous. Such a result suggests that the activation of the carbon spheres at 1123 K does not cause detectable phase change from amorphous phase to crystalline phase.

Fig. 3 depicts the XRD patterns of the AC spheres. There is a broad peak at 20° for all the AC spheres, indicating the amorphous state of all the AC spheres. The small peak at ~43° corresponds to

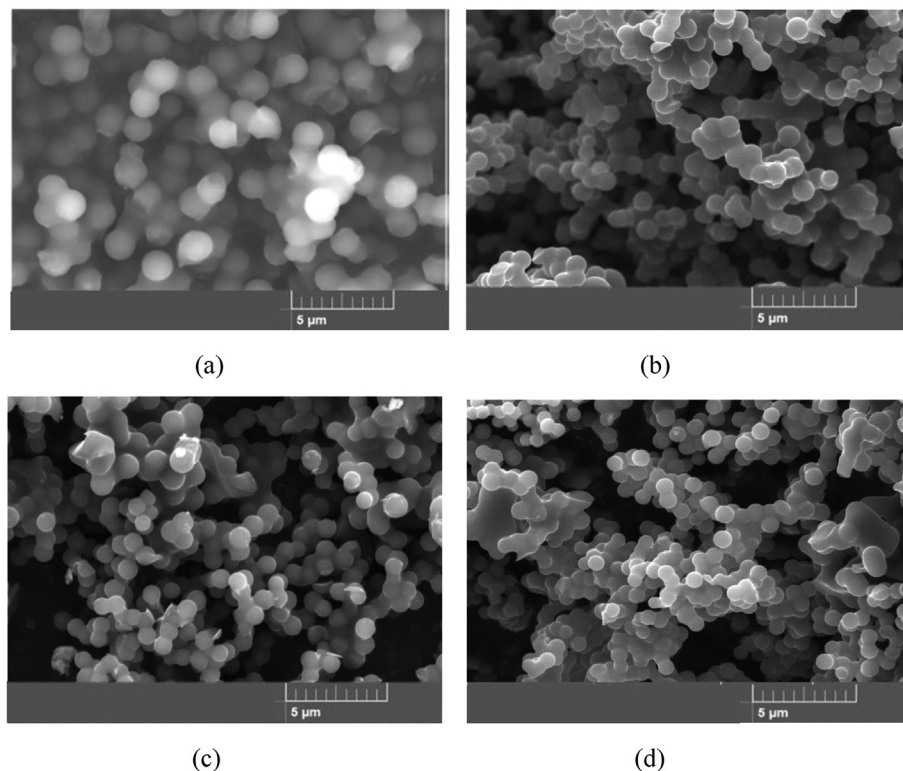


Fig. 1. SEM images of carbon spheres made from HFC555 via HTC and physical activation; (a) without activation (AC-0), (b) with activation of 2 h (AC-2), (c) with activation of 3 h (AC-3), and (d) with activation of 4 h (AC-4).

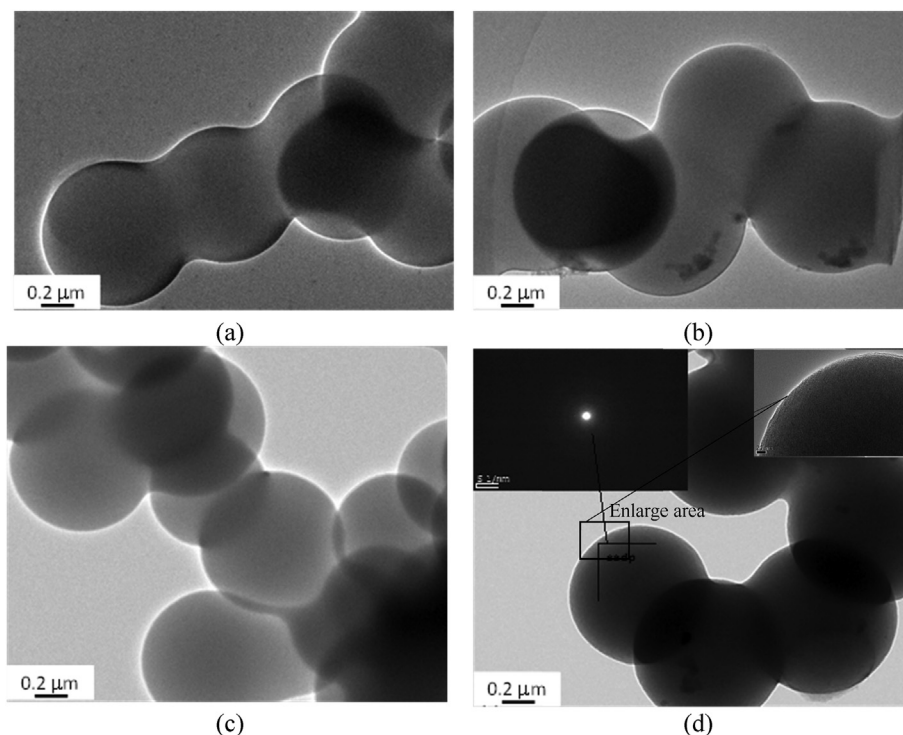


Fig. 2. TEM images of carbon spheres heat-treated with different activation times; (a) 1 h (AC-1), (b) 2 h (AC-2), (c) 3 h (AC-3), and (d) 4 h (AC-4).

the (100) plane of graphitic carbon, suggesting low graphitization of AC spheres.

The surface chemistry of the AC spheres was examined by FTIR. Fig. 4 shows the FTIR spectra of the AC spheres. It is evident that increasing the activation time leads to the increase of transmittance

at the wavenumber of 2166 cm^{-1} , which likely reveals the presence of the $\text{—C}\equiv\text{C—}$ stretch. There is a weak peak for the wavenumber in the range of $1600\text{--}1700\text{ cm}^{-1}$, corresponding to the $\text{C}=\text{C}$ bond stretching vibration. There are no peaks associated with C—N , C=O or C—H bond. Such a result suggests that most residuals/impurities

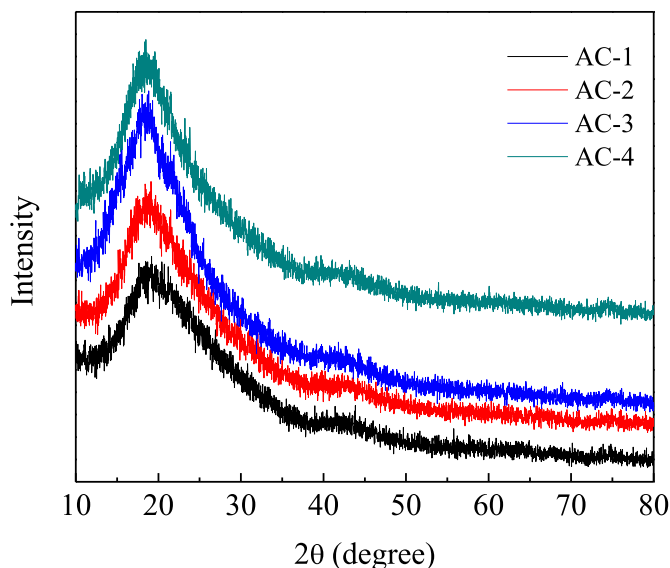


Fig. 3. XRD patterns of AC spheres.

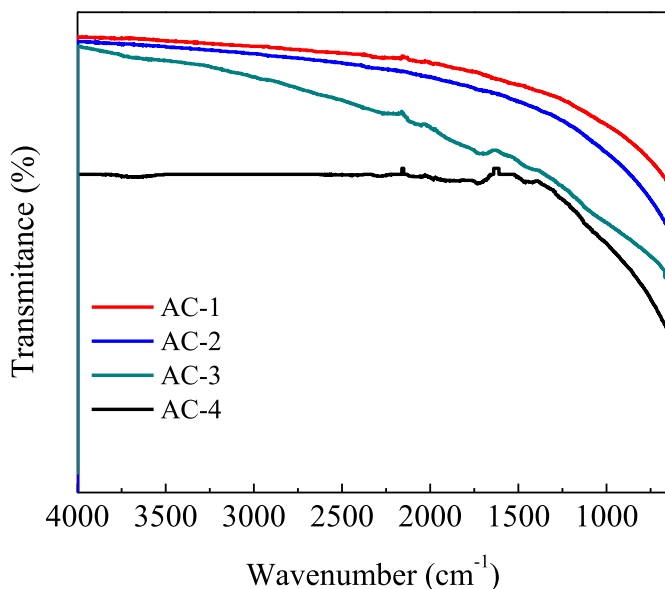


Fig. 4. FTIR spectra of AC spheres.

left from the HTC process have been removed during the physical self-activation at 1123 K with the activation time more than or equal to 1 h. There are no functional groups on the surface of the AC spheres.

To determine the porous characteristics of the AC spheres, the nitrogen adsorption–desorption isotherms were measured by an automated gas adsorption analyzer (Micromeritics surface characterization, Norcross, GA). Fig. 5a shows the nitrogen adsorption–desorption isotherms of the AC spheres of AC-x (x: 1, 2, 3, and 4). The isotherms of all the AC spheres show a combination of Type I and Type II features [41]. There is a rapid increase of the adsorbed quantity in the range of low relative pressure, which is associated with the filling of micropores. This trend is the characteristic of Type I structure, indicating the presence of microporous structure. After the stage of rapid adsorption, the adsorbed quantity increases slowly with the increase of the relative pressure, showing the characteristic of Type II structure. Such behavior suggests the

presence of macroporous structure. The hysteresis and the increase of the adsorbed quantity with the increase of the relative pressure reveal the presence of some mesoporosity. Note that the slope of the adsorbed quantity vs relative pressure is associated with the filling of mesopores.

Fig. 5b shows the distribution of the pore sizes of the AC spheres of AC-x, which was calculated by the DFT (density functional theory) method. The AC spheres of AC-1 exhibits relatively mono-disperse distribution with the largest differential pore volume at the pore size of 1.68 nm; the AC-2 exhibits bimodal distribution with the largest differential pore volume at the pore size of 1.68 nm, the AC spheres of both AC-3 and AC-4 have a similar distribution of pore sizes with the largest differential pore volume at the pore size of ~0.66 nm. Such a trend reveals that increasing the activation time from 1 h to 4 h leads to the decrease of the average pore size and the fraction of mesopores.

Table 1 summarizes the surface characteristics of the AC spheres of AC-x. Two different methods were used to calculate the total surface area; one is the BET method with the calculated total surface area as S_{BET} , and the other is the DFT method with the calculated total surface area as S_{DFT} . The total pore volume was calculated at a relative pressure of 0.99. The DFT method was used to calculate the surface areas (S_{micro} and S_{meso}) and pore volumes (V_{micro} and V_{meso}) of the micropores and mesopores. Note that $S_{\text{DFT}} = S_{\text{meso}} + S_{\text{micro}}$ and $V_{\text{total}} = V_{\text{meso}} + V_{\text{micro}}$ (V_{total} : total pore volume).

From Table 1, one can note that the total surface area of S_{BET} increases from 399 m^2/g to 1364 m^2/g , and the ratio of $S_{\text{micro}}/S_{\text{DFT}}$ increases from 61% to 90% with the increase of the activation time from 1 h to 3 h. There is no significant difference of the surface parameters between the AC spheres of AC-3 and AC-4. Such a trend suggests the important role of the activation time in controlling the evolution of the porous structures of ACs for the activation of carbonized materials at high temperatures. There likely exists a threshold for the activation time, above which the activation will not significantly change the characteristics of the porous structures of ACs. It is worth mentioning that the threshold of the activation time is dependent on the activation conditions and the structures of carbonized materials.

It is noted that the AC spheres of AC-4 have the largest total surface area and the surface area of micropores, and the AC spheres of AC-3 has larger S_{micro} and V_{micro} than AC-4. The more the amount of micropores, the higher is the total surface area.

3.2. Electrochemical performance of activated carbon spheres

Fig. 6 shows the Nyquist plots of the AC spheres of AC-x, in which a semicircle and a spike appear in the high and low frequency regions, respectively. The semicircle suggests that the electron motion is the dominant mechanism controlling the electrical conductivity of the AC spheres in 6 M KOH in the high frequency region, and the AC spheres exhibit resistive characteristic. The spike reveals the capacitive behavior of electric double layer in the AC spheres in the low frequency region. There is a transition between these two regions for medium frequency, in which both ionic transport and electron motion determine the electrical conductivity of the AC spheres. It is worth mentioning that multiple EIS measurements (>4) were performed for the same conditions. All the EIS results exhibit similar trend, which suggests that the Nyquist plots of the AC spheres reveal the impedance characteristics of the AC spheres of AC-x.

In general, the electrochemical impedance of a supercapacitor can be described by a lumped element model [42], consisting of 1) series resistance (R_s), depending on the electrolyte conductivity and the intrinsic resistance of separator, 2) AC/electrolyte interfacial impedance of capacitance (C_{dl}), resistance to charge transfer

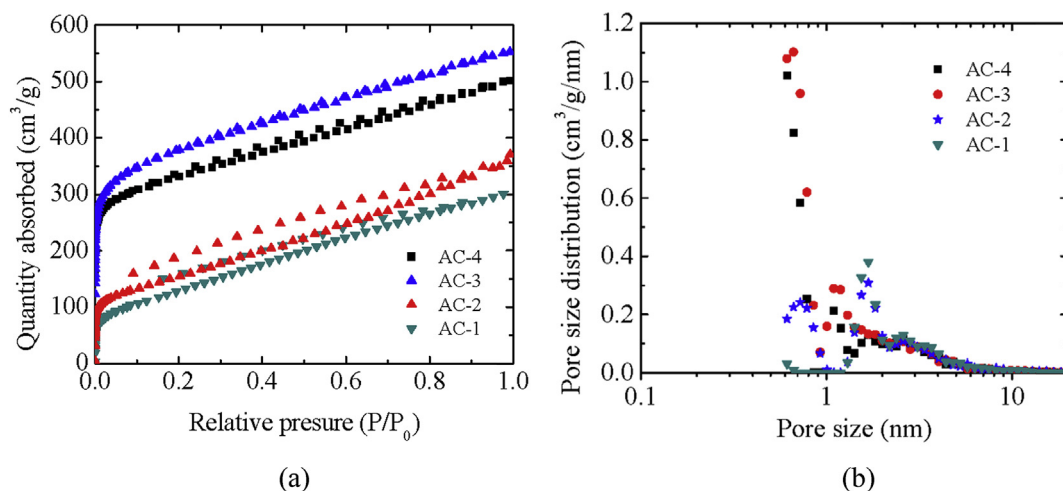


Fig. 5. Adsorption behavior of AC spheres of AC-x (x: 1, 2, 3, and 4): (a) nitrogen adsorption-desorption isotherms, and (b) distribution of the pore sizes calculated from the adsorption isotherms via the DFT (density functional theory) method.

Table 1
Porous parameters of AC-x.

	Average pore diameter (nm)	S_{BET} (m ² /g)	S_{DFT} (m ² /g)	V_{total} (cm ³ /g)	S_{micro} (m ² /g) (area%)	S_{meso} (m ² /g) (area%)	V_{micro} (cm ³ /g) (vol%)	V_{meso} (cm ³ /g) (vol%)
AC-1	5.5	399	433	0.55	264 (61)	169 (39)	0.19 (35)	0.36 (65)
AC-2	4.5	509	543	0.57	395 (73)	148 (27)	0.26 (46)	0.31 (54)
AC-3	2.5	1364	1429	0.86	1280 (90)	149 (10)	0.50 (58)	0.36 (42)
AC-4	2.5	1223	1473	0.76	1328 (90)	145 (10)	0.44 (58)	0.33 (42)

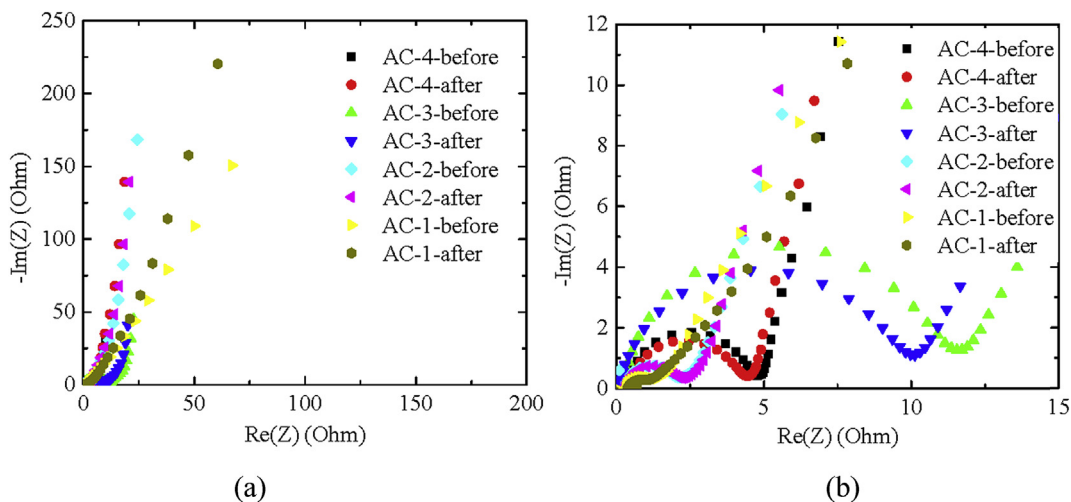


Fig. 6. (a) Nyquist plot of the AC spheres of AC-x before and after 50 cycles of CV test and 60 cycles of GC test, and (b) enlarged view of the Nyquist plot of (a) in the high frequency range.

(R_{ct}), and the Warburg impedance, and 3) the capacitance and resistance associated with the defects of current collector and separator. Using a lumped element model to analyze the Nyquist plots of the AC spheres of AC-x in both the low and high frequency regions, one obtains the values of the individual elements.

Table 2 lists the fitting values of the R_s , R_{ct} and C_{dl} of the supercapacitors made from the AC spheres of AC-x before and after the cycling tests (50 cycles of CV test and 60 cycles of GC test). Here, the characteristic time, τ , is calculated as $R_{\text{ct}}C_{\text{dl}}$, which is a function of average pore size and associated with the ionic motion in small

Table 2
Fitting values of R_s , R_{ct} and C_{dl} of the supercapacitors made from the AC spheres of AC-x before and after the cycling tests (50 cycles of CV test and 60 cycles of GC test).

	1h		2h		3h		4h	
	before	after	before	after	before	after	before	after
R_s (ohm)	0.31	0.31	0.31	0.32	0.28	0.25	0.42	0.46
R_{ct} (ohm)	2.77	2.83	1.64	1.69	10.83	8.30	4.16	3.61
C_{dl} (μF)	20.30	19.80	14.60	14.10	17.41	23.22	20.63	24.42
τ (μs)	56.23	56.03	23.94	23.83	188.55	192.73	85.82	88.16

pores. It is evident that there are no significant differences of the values of four parameters for the supercapacitor cells before and after the cycling tests. The cycling tests have no significant effect on the values of these four parameters. The supercapacitors made from the AC spheres of AC-3 have the smallest R_s , the largest R_{ct} , and τ in accord with the distribution of the pore sizes in Fig. 2b.

A knee frequency is defined as the initial frequency for the transition from the predominantly resistive behavior to the predominantly capacitive behavior [43,44]. For frequency less than the knee frequency, ions (K^+) in electrolyte undergo directional migration to accumulate inside the pores of AC spheres, and the supercapacitor cell exhibits a good capacitive behavior. That is to say, a large knee frequency is preferable. The variation of the normalized capacitance with frequency is shown in Fig. 7, in which the capacitance is normalized by the corresponding capacitance at the frequency of 0.02 Hz. The normalized capacitance decreases with increasing frequency, and there is a sharp decrease of the capacitance in the frequency range of 0.2–0.6 Hz. From Fig. 7, the knee frequency is determined as the frequency at which the normalized capacitance is 0.8 [43,44]. The knee frequencies of the supercapacitors made from the AC spheres of AC-x are 0.14, 0.13, 0.079 and 0.067 Hz for the AC spheres of AC-4, AC-2, AC-3, and AC-1, respectively. The supercapacitors made from the AC spheres of AC-4 and AC-2 exhibit better capacitive characteristics than the other two. It needs to point out that the knee frequency is dependent on the microstructure of AC spheres, electrolyte, separator, and the assembling of the supercapacitor cells.

Fig. 8a shows the IV (current and voltage) curves of the supercapacitor cells made from the AC spheres of AC-1 for various scan rates. The quasi-rectangular shape of the IV curves suggests a good capacitive behavior of the supercapacitor cells and good stability of the AC spheres in the aqueous KOH electrolyte. The large enclosed area and the steep charge and discharge segments reveal that the supercapacitor cells possess excellent electrochemical performance. Note that increasing the scan rate leads to the deviation of the IV curves from rectangular shape, which is likely due to the presence of the characteristic time of τ associated with the migration and accumulation of ions. In general, the resistance to ionic motion and the resultant force acting onto the ions accumulated near the surfaces of pores are functions of local electric field (current density). The increase in the scan rate leads

to temporal change of local electric field (current density), and alter the motion of ions in and near pores. This trend causes the deviation of the IV curves from the ideal shape of rectangle, and the deviation from the ideal shape of rectangle increases with the increase of the scan rate.

The specific capacitance of one single electrode for a two-electrode supercapacitor system can be calculated from both CV and GC measurements. Using the IV curves, the specific gravimetric capacitance (SGC) in the unit of F/g is calculated as [45,46].

$$C = \frac{2I}{mv} \quad (1)$$

where I (A) is the electric current intensity, m (g) is the mass of single electrode, v (V/s) is the scan rate. The average specific gravimetric capacitance (F/g) can be calculated from the integration of voltammetric charge as

$$C = \frac{1}{mv} \frac{\int I(V)dV}{\Delta V} \quad (2)$$

where ΔV is the voltage window. Note that the mass can be replaced with area or volume, which gives the specific areal capacitance and the specific volumetric capacitance.

Using Eq [1] and the IV curves, one can obtain the CV (capacitance and voltage) curves, which reveals the capacitance change during charging-discharging cycles. Fig. 8b–e shows the CV curves of the supercapacitor cells made from the AC spheres of AC-x at tenth cycle for the scan rate in the range of 2–100 mV/s. All the CV curves are presented in quasi-rectangular shape, indicating that all the AC spheres of AC-x possess microporous structures in accord with the measurement of the nitrogen adsorption–desorption isotherms and good capacitive characteristic for the charge storage. One can note that the CV curve at the smallest scan rate of 2 mV/s exhibits a spike at the voltage of 1 V for all the supercapacitor cells. The magnitude of the spike decreases with the increase of the scan rate. For the scan rate of 100 mV/s, the CV curves become more symmetric, and the spike at the voltage of 1 V nearly disappears. Such behavior reveals the presence of fast charging and discharging in the form of non-Faradic current at high scan rates.

Fig. 8f shows the rate dependence of normalized capacitance of the supercapacitor cells made from the AC spheres of AC-x, in which the capacitance of the corresponding supercapacitor cells measured at the scan rate of 2 mV/s was used in the normalization. Note that all the capacitances used in the calculation of the normalized capacitance is the average specific gravimetric capacitance at tenth cycle, and the average specific gravimetric capacitances of the tenth cycle at the scan rate of 2 mV/s are 124, 133, 154 and 164 F/g for the supercapacitor cells made from the AC spheres of AC-1, AC-2, AC-3 and AC-4, respectively. It is evident that the supercapacitor cells made from the AC spheres of AC-2, which have the smallest τ , have the best rate dependence with 79.6% of 133 F/g at the scan rate of 100 mV/s, and the supercapacitor cells made from the AC spheres of AC-3 and AC-4 exhibit similar trend with ~70% of 154 and 164 F/g, respectively, at the scan rate of 100 mV/s. It is worth mentioning that there are a variety of factors controlling the rate dependence of the capacitance of a supercapacitor, including the distribution of pore sizes, connection of pores, surface properties, etc.

Galvanostatic charging and discharging measurements of the supercapacitor cells made from the AC spheres of AC-x were performed for electric current density in a sequence of 0.2–10 A/g with a voltage window of 0–1 V. For the GC tests, the specific gravimetric capacitance (SGC) is calculated as

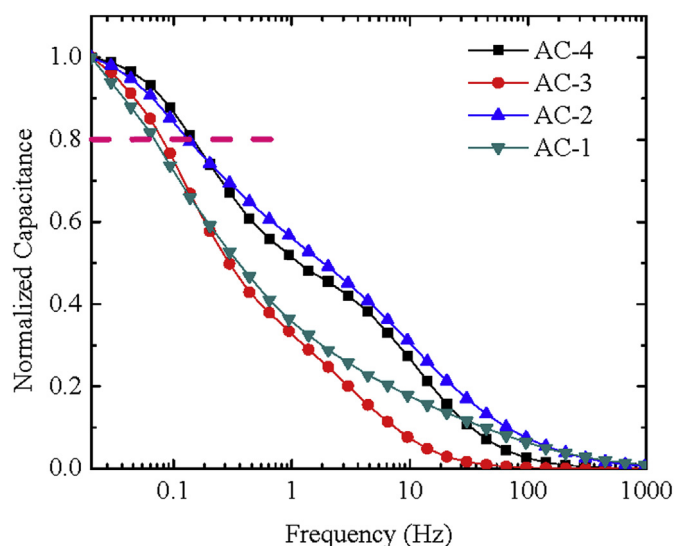


Fig. 7. Variation of normalized capacitance with frequency for the supercapacitor cells made from the AC spheres of AC-x.

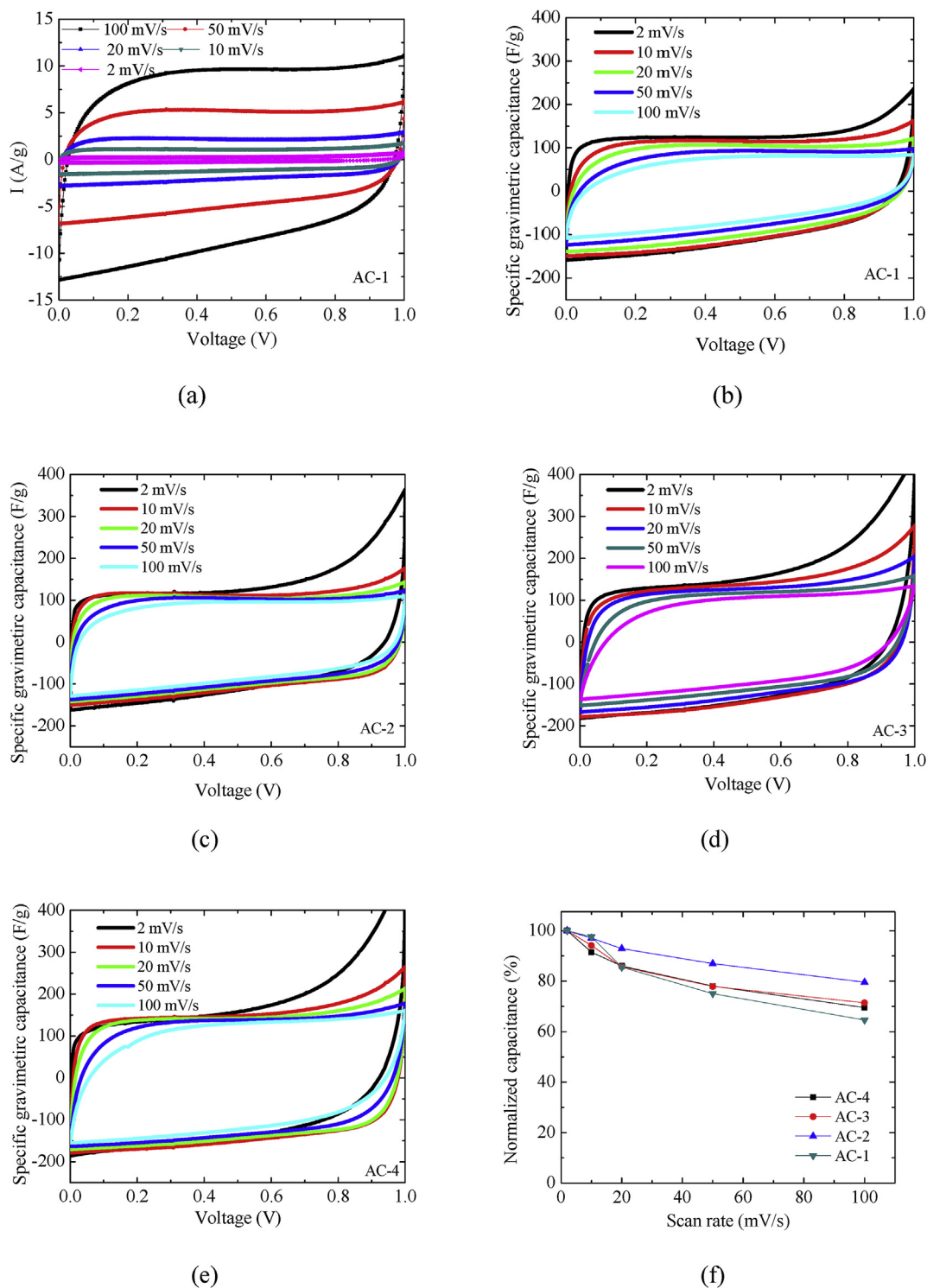


Fig. 8. Electrochemical properties of the supercapacitor cells made from the AC spheres of AC-x at tenth cycle; (a) IV curves of AC-1, (b)–(e) CV curves of AC-x, and (f) rate dependence of normalized capacitance of AC-x.

$$C = \frac{4i}{\Delta V / \Delta t} \quad (3)$$

where i is the electric current density related to total mass of both electrodes, and $\Delta V / \Delta t$ is the slope of the discharging curve after the IR drop.

Fig. 9a shows the GC curves of the supercapacitor cells made from the AC spheres of AC-x at tenth cycle for an electric current density of 0.5 A/g. The GC curves display triangle-like shape with reasonable symmetry, indicating good capacitive behavior of all the supercapacitor cells made from the AC spheres of AC-x. There exists an IR drop at the onset of the discharging, indicating the energy loss

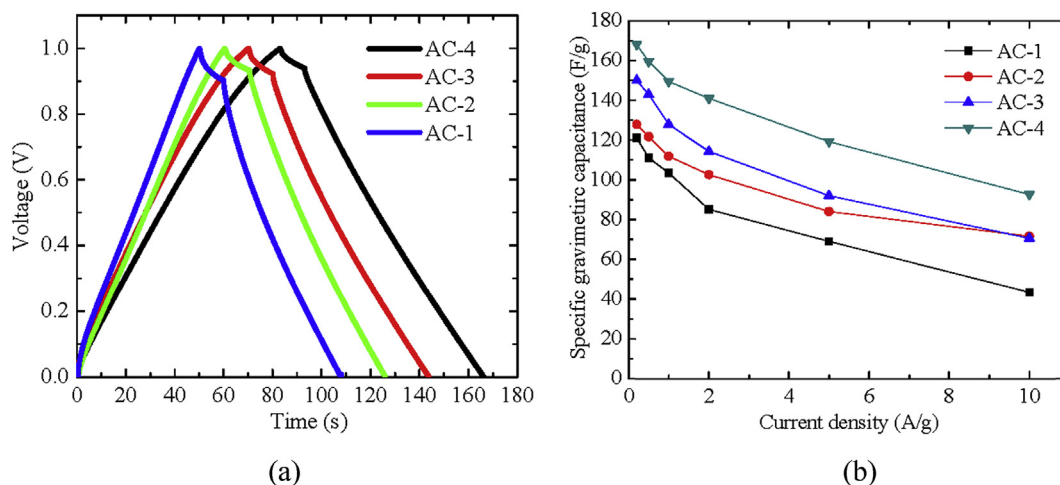


Fig. 9. (a) GC curves of the supercapacitor cells made from the AC spheres of AC-x at tenth cycle for an electric current density of 0.5 A/g, and (b) variation of SGC with electric current density.

associated with the internal resistance of the supercapacitor cells. The SGCs are 111.1, 121.7, 142.9, and 159.5 F/g for the AC spheres of AC-1, AC-2, AC-3 and AC-4, respectively, compatible with the results from the CV measurement. Such a trend again demonstrates the importance of the activation time in determining the electrochemical performance of the supercapacitors made from ACs.

Fig. 9b shows the variation of the SGC measured from the GC test with electric current density for the supercapacitor cells made from the AC spheres of AC-x. The SGC of all the supercapacitor cells decreases with the increase of electric current density, suggesting the effect of electric current density on the motion of ions and the energy storage. The larger the electric current density, the less is the ions accumulated at the electrolyte/electrode interface.

The supercapacitor cells made from the AC spheres of AC-4 have the largest SGC at the corresponding electric current density, which decreases from 168 F/g for the electric current density of 0.2 A/g to 159.5 F/g and 92.6 F/g for the electric current densities of 0.5 and 10 A/g, respectively. The supercapacitor cells made from AC-1 have the smallest SGC. The largest decrease of the SGC for all the supercapacitor cells occurred for small electric current density. This trend suggests that there likely exists the effect of electric field (current) on the motion of ions, i.e. the electrophoretic velocity of ions, near the interfaces between electrolyte and AC spheres. The larger the electric current density, the larger is the driving force for the motion of ions. The interaction between AC spheres and the ions in electrolyte likely cannot counterbalance

the driving force on the ions, and more ions can easily move away AC spheres and migrate back to the electrolyte. This causes the reduction of ions accumulated in the AC spheres and the decrease of the capacitance.

Table 3 summarizes the surface properties and specific gravimetric capacitance of the AC spheres of AC-4. For comparison, the surface properties and specific gravimetric capacitance of some ACs reported in the literature are also included in Table 3. It is evident that the AC spheres of AC-4 have the largest SSA and pore volume in comparison with the ACs made from other biomass via physical activation, and the SGC is compatible with the ACs made from coffee endocarp [47] with physical activation and coconut kernel pulp [38] with chemical activation. Such a trend suggests the feasibility and practicality of the self-physical activation.

The effect of electrochemical cycling on the capacitive behavior of the supercapacitor cells made from the AC spheres of AC-x was studied for the charging-discharging cycles up to 2000 at an electric current density of 0.5 A/g. Fig. 10 shows the effect of charging-discharging cycle on the capacitive behavior of the supercapacitor cells at the electric current density of 0.5 A/g. For the supercapacitor cells made from AC-1 and AC-2, the specific gravimetric capacitance decreases relatively fast for the first few cycles, and the cells approach relatively stable state with small decrease in the capacitance with the increase of the cycle number. For the supercapacitor cells made from AC-3 and AC-4, the specific gravimetric capacitance decreases relatively slowly with the increase of the cycle number and approaches plateau. The supercapacitor cells made

Table 3

Surface properties and specific gravimetric capacitance of biomass-derived activated carbons as the electrodes of supercapacitors.

Biomass	SSA (m ² /g)	Pore volume (cm ³ /g)	Activation method (agent)	Electrolyte	SGC (F/g)
Cherry stones [37]	1273	—	Chemical (KOH)	H ₂ SO ₄	232
Fish scale [48]	2273	2.74	Chemical (KOH)	KOH	168
Pig bone [48]	2157	2.26	Chemical (KOH)	KOH	185
Sunflower seed shell [48]	2585	1.41	Chemical (KOH)	KOH	311
Waste paper [48]	526	—	Chemical (KOH)	KOH	180
Wood sawdust [48]	2967	1.35	Chemical (KOH)	Organic	236
Hemp [34,35]	2287	1.45	Chemical (KOH)	Liquid	142
Coconut kernel pulp [38]	1200	0.60	Chemical (KOH)	H ₂ SO ₄	173
Pistachio shell [49]	1009	0.67	Physical (Steam)	NaNO ₃	80
Fire woods [49]	1016	0.75	Physical (Steam)	NaNO ₃	105
Corn cob [36]	1210	0.67	Physical (Steam)	KOH	314
Coffee endocarp [47]	1050	0.5	Physical (CO ₂)	H ₂ SO ₄	176
HFCS (this work)	1364	0.86	Self-Physical	KOH	168

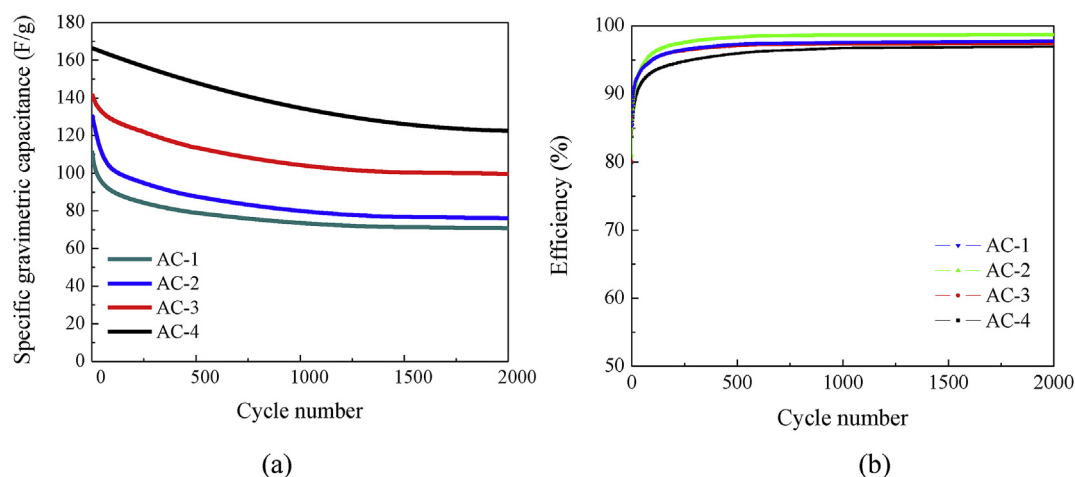


Fig. 10. Effect of charging-discharging cycle on capacitive behavior of the supercapacitor cells made from the AC spheres of AC-x (electric current density: 0.5 A/g); (a) SGCR retention, and (b) efficiency.

from the AC spheres of AC-4 have the largest specific gravimetric capacitance, and the supercapacitor cells made from the AC spheres of AC-1 have the smallest specific gravimetric capacitance. This result reveals the importance of the porous structures in the energy storage. The AC spheres of AC-4 have the largest fraction of micropores, and the AC spheres of AC-1 have the least fraction of micropores.

Fig. 10b shows the variation of the Coulombic efficiency of the supercapacitor cells. The Coulombic efficiency increases with the increase of the cycle number, and approaches about 100%, indicating a highly reversible adsorption/desorption of K^+ ions on the surfaces of the pores of AC spheres and a prosperous cycle-life. Note that the supercapacitor cells made from the AC spheres of AC-2 has the highest Coulombic efficiency, while supercapacitor cells made from the AC spheres of AC-4 has the lowest Coulombic efficiency. It is known that the Coulombic efficiency represents the cyclic stability of electrode materials. The results shown in Fig. 10b indicate good stability of the AC spheres of AC-x.

The specific energy density and power density were calculated from the CV curves to further analyze the electrochemical

performance of the supercapacitor cells made from the AC spheres of AC-x, using Eq. (4)

$$E(W \cdot h/kg) = \frac{C(\Delta V)^2}{8 \cdot 3.6} \text{ and } P(W/kg) = 3600 \frac{VE}{\Delta V} \quad (4)$$

Fig. 11 shows the Ragone plot of the supercapacitor cells made from the AC spheres of AC-x. It is evident that increasing the power density leads to the decrease of the energy density. Generally, both the energy density and power density of supercapacitor depend on the characteristics of porous structures and the chemophysical properties of the electrode material. As discussed above, increasing the scan rate will cause the decrease of the capacitance due to the increase in the resistance to the ionic motion and the decrease of the accumulation of ions at the electrolyte/electrode interfaces. For the same porous structures, it is impossible to increase the energy density and the power density simultaneously. Supercapacitors using electrode materials of optimal porous structures need to be explored, as revealed in Fig. 11 that the supercapacitor cells made from the AC spheres of AC-3 and AC-4 have approximately the largest energy density for the same power density. The more the micropores, the larger is the energy density at the same power density for the supercapacitors with aqueous electrolytes.

4. Summary

In summary, activated carbons of spherical shape were prepared with high fructose corn syrup as the precursor via hydrothermal processing and physical self-activation. The effect of the activation time on the geometrical and porous characteristics was investigated. The size of the prepared AC spheres is about 0.8 μm , independent of the activation time, and the surface area of micropores increases with increasing the activation time. Increasing the activation time leads to the increase of the fraction of micropores with the pore size of ~ 0.67 nm.

Using the AC spheres as electrode materials, supercapacitor cells of symmetrical type (two-electrodes) were prepared without any additives and binders. The electrochemical performance of the supercapacitor cells was characterized. The supercapacitor cells made from the AC spheres of AC-4 exhibit excellent electrochemical performance with a specific capacitance of 168 F/g at an electric current density of 0.2 A/g and an energy density of 4.2 W h/kg at a power density of 1.5 kW/kg. Increasing the surface area and fraction

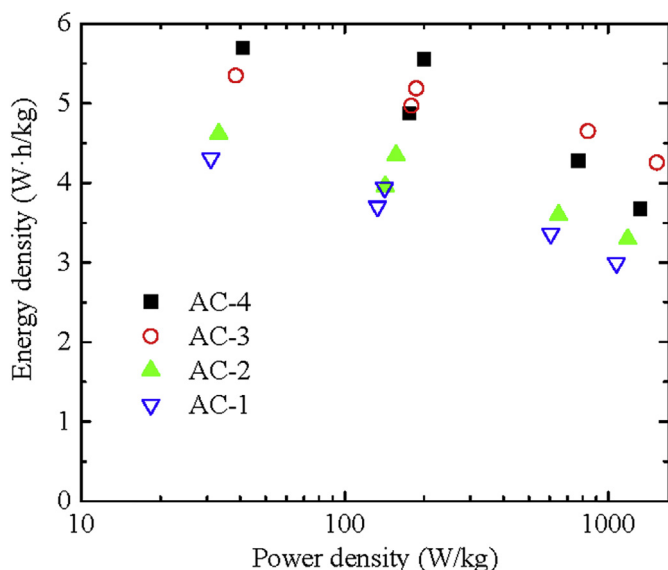


Fig. 11. Ragone plot of the supercapacitor cells made from the AC spheres of AC-x.

of the micropores leads to the increase of the specific gravimetric capacitance.

Acknowledgements

This work is supported by the NSF through the grant CMMI-1634540, monitored by Dr. Khershed Cooper. We also thank Dr. Wanggang Zhang of Taiyuan University of Technology for conducting the microstructure analysis and Prof. Meiqing Guo of Taiyuan University of Technology for conducting surface area analysis.

Appendix A. Supplementary data

Supplementary data related to this article can be found at <https://doi.org/10.1016/j.mtener.2018.07.002>.

References

- [1] H. Jiang, P.S. Lee, C. Li, *Energy Environ. Sci.* 6 (2013) 41.
- [2] P. Simon, Y. Gogotsi, *Nat. Mater.* 7 (2008) 845.
- [3] H. Zhang, X. Zhang, Y. Ma, *Electrochim. Acta* 184 (2015) 347.
- [4] E. Raymundo-Pinero, K. Kierzek, J. Machnikowski, F. Béguin, *Carbon* 44 (2006) 2498.
- [5] J. Wang, S. Kaskel, *J. Mater. Chem.* 22 (2012) 23710.
- [6] J. Huang, B.G. Sumpter, V. Meunier, *Chemistry* 14 (2008) 6614.
- [7] J.J. Niu, J.N. Wang, Y. Jiang, L.F. Su, J. Ma, *Microporous Mesoporous Mater.* 100 (2007) 1.
- [8] Y. Dai, H. Jiang, Y. Hu, Y. Fu, C. Li, *Ind. Eng. Chem. Res.* 53 (2014) 3125.
- [9] H. Zhang, G. Cao, Z. Wang, Y. Yang, Z. Shi, Z. Gu, *Electrochem. Commun.* 10 (2008) 1056.
- [10] A.V. Murugan, T. Muraliganth, A. Manthiram, *Chem. Mater.* 21 (2009) 5004.
- [11] S. Chen, W. Cai, R.D. Piner, J.W. Suk, Y. Wu, Y. Ren, J. Kang, R.S. Ruoff, *Nano Lett.* 11 (2011) 3519.
- [12] S. Stankovich, D.A. Dikin, R.D. Piner, K.A. Kohlhaas, A. Kleinhammes, Y. Jia, Y. Wu, S.T. Nguyen, R.S. Ruoff, *Carbon* 45 (2007) 1558.
- [13] Y. Zhu, S. Murali, M.D. Stoller, A. Velamakanni, R.D. Piner, R.S. Ruoff, *Carbon* 48 (2010) 2118.
- [14] W. Lv, D.-M. Tang, Y.-B. He, C.-H. You, Z.-Q. Shi, X.-C. Chen, C.-M. Chen, P.-X. Hou, C. Liu, Q.-H. Yang, *ACS Nano* 3 (2009) 3730.
- [15] Y. Sun, Q. Wu, G. Shi, *Energy Environ. Sci.* 4 (2011) 1113.
- [16] B. Luo, S. Liu, L. Zhi, *Small* 8 (2012) 630.
- [17] J. Xia, F. Chen, J. Li, N. Tao, *Nat. Nanotechnol.* 4 (2009) 505.
- [18] W. Xiong, M. Liu, L. Gan, Y. Lv, Y. Li, L. Yang, Z. Xu, Z. Hao, H. Liu, L. Chen, *J. Power Sources* 196 (2011) 10461.
- [19] Z. Gao, N. Song, Y. Zhang, X. Li, *Nano Lett.* 15 (2015) 8194.
- [20] Z. Gao, Y. Zhang, N. Song, X. Li, *Electrochim. Acta* 246 (2017) 507.
- [21] Z. Gao, Y. Zhang, N. Song, X. Li, *Mater. Res. Lett.* 5 (2016) 69.
- [22] L. Wei, M. Sevilla, A.B. Fuertes, R. Mokaya, G. Yushin, *Adv. Energy Mater.* 1 (2011) 356.
- [23] X. Li, C. Han, X. Chen, C. Shi, *Microporous Mesoporous Mater.* 131 (2010) 303.
- [24] X. Li, W. Xing, S. Zhuo, J. Zhou, F. Li, S.-Z. Qiao, G.-Q. Lu, *Bioresour. Technol.* 102 (2011) 1118.
- [25] V. Subramanian, C. Luo, A.M. Stephan, K.S. Nahm, S. Thomas, B. Wei, *J. Phys. Chem. C* 111 (2007) 7527.
- [26] D. Kalpana, S.H. Cho, S.B. Lee, Y.S. Lee, R. Misra, N.G. Renganathan, *J. Power Sources* 190 (2009) 587.
- [27] W. Huang, H. Zhang, Y. Huang, W. Wang, S. Wei, *Carbon* 49 (2011) 838.
- [28] W. Chen, H. Zhang, Y. Huang, W. Wang, *J. Mater. Chem.* 20 (2010) 4773.
- [29] K.S. Ro, K.B. Cantrell, P.G. Hunt, *Ind. Eng. Chem. Res.* 49 (2010) 10125.
- [30] J. Lehmann, *Nature* 447 (2007) 143.
- [31] F.P. Vaccari, S. Baronti, E. Lugato, L. Genesio, S. Castaldi, F. Fornasier, F. Miglietta, *Eur. J. Agron.* 34 (2011) 231.
- [32] S.P. Galinato, J.K. Yoder, D. Granatstein, *Energy Pol.* 39 (2011) 6344.
- [33] L. Wang, Y. Guo, B. Zou, C. Rong, X. Ma, Y. Qu, Y. Li, Z. Wang, *Bioresour. Technol.* 102 (2011) 1947.
- [34] H. Wang, Z. Xu, A. Kohandehghan, Z. Li, K. Cui, X. Tan, T.J. Stephenson, C.K. King'ondo, C.M. Holt, B.C. Olsen, *ACS Nano* 7 (2013) 5131.
- [35] W. Sun, S.M. Lipka, C. Swartz, D. Williams, F.Q. Yang, *Carbon* 103 (2016) 181.
- [36] W.-H. Qu, Y.-Y. Xu, A.-H. Lu, X.-Q. Zhang, W.-C. Li, *Bioresour. Technol.* 189 (2015) 285.
- [37] M. Olivares-Marín, J.A. Fernández, M.J. Lázaro, C. Fernández-González, A. Macías-García, V. Gómez-Serrano, F. Stoeckli, T.A. Centeno, *Mater. Chem. Phys.* 114 (2009) 323.
- [38] B. Kishore, D. Shanmugasundaram, T.R. Penki, N. Munichandraiah, *J. Appl. Electrochem.* 44 (2014) 903.
- [39] J.S. White, *Am. J. Clin. Nutr.* 88 (2008) 1716S.
- [40] X.-X. Lin, B. Tan, L. Peng, Z.-F. Wu, Z.-L. Xie, *Mater. Chem.* 4 (2016) 4497.
- [41] X. Yang, J. Yu, W. Zhang, G. Zhang, *RSC Adv.* 7 (2017) 15096.
- [42] C. Lei, F. Markoulidis, Z. Ashitaka, C. Lekakou, *Electrochim. Acta* 92 (2013) 183.
- [43] B.E. Conway, *Electrochemical Supercapacitors: Scientific Fundamentals and Technological Applications*, Springer Science & Business Media, 2013.
- [44] P. Taberna, P. Simon, J.-F. Fauvarque, *J. Electrochem. Soc.* 150 (2003) A292.
- [45] B. Anothumakkool, S.N. Bhange, S.M. Unni, S. Kurungot, *RSC Adv.* 3 (2013) 11877.
- [46] J. Chmiola, G. Yushin, R. Dash, Y. Gogotsi, *J. Power Sources* 158 (2006) 765.
- [47] J.M. Nabais, J.G. Teixeira, I. Almeida, *Bioresour. Technol.* 102 (2011) 2781.
- [48] J. Wang, S. Kaskel, *J. Mater. Chem.* 22 (2012).
- [49] F.-C. Wu, R.-L. Tseng, C.-C. Hu, C.-C. Wang, *J. Power Sources* 144 (2005) 302.